GRADUATE AERONAUTICAL LABORATORIES
CALIFORNIA INSTITUTE OF TECHNOLOGY

Experiments and modeling of impinging laminar jets at moderate separation distances

Jeffrey M. Bergthorson, Kazuo Sone, Trent W. Mattner,
Paul E. Dimotakis, David G. Goodwin, and Dan I. Meiron

GALCIT Report GALCITFM2005.003

16 MAY 2005

Firestone Flight Sciences Laboratory

Guggenheim Aeronautical Laboratory

Karman Laboratory of Fluid Mechanics and Jet Propulsion

Pasadena

Experiments and modeling of impinging laminar jets at moderate separation distances

Jeffrey M. Bergthorson*, Kazuo Sone, Trent W. Mattner,
Paul E. Dimotakis, David G. Goodwin and Dan I. Meiron
California Institute of Technology
Pasadena, California 91125

16 May 2005

Abstract

This report describes an experimental and numerical study of impinging, incompressible, axisymmetric, laminar jets, where the jet axis of symmetry is aligned normal to the wall. Particle Streak Velocimetry (PSV) is used to measure axial velocities along the centerline of the flow field. The jet-nozzle pressure drop is measured simultaneously and determines the Bernoulli velocity. The flowfield is simulated numerically by an axisymmetric Navier-Stokes spectral-element code, an axisymmetric potential-flow model, and an axisymmetric one-dimensional streamfunction approximation. The axisymmetric viscous and potential-flow simulations include the nozzle in the solution domain, allowing nozzle-wall proximity effects to be investigated. Scaling the centerline axial velocity by the Bernoulli velocity collapses the experimental velocity profiles onto a single curve that is independent of the nozzle-plate separation distance. Axisymmetric direct numerical simulations yield good agreement with experiment and confirm the velocity profile scaling. Potential-flow simulations reproduce the collapse of the data, however, viscous effects result in disagreement with experiment. Axisymmetric one-dimensional streamfunction simulations can predict the flow in the stagnation region if the boundary conditions are correctly specified. The scaled axial velocity profiles are well-characterized by an error function with one Reynolds-number dependent parameter. Rescaling the wall-normal distance by the boundary-layer displacement-thickness-corrected diameter yields a collapse of the data onto a single curve that is independent of the Reynolds number. These scalings allow the specification of an analytical expression for the velocity profile of an impinging laminar jet over the Reynolds number range investigated of $200 \leq Re \leq 1400$.

*Corresponding author.
E-mail address: jeffb@tyrvos.caltech.edu

1 Introduction

Axisymmetric jets impinging perpendicularly on a wall are encountered in a variety of contexts, from large-scale applications of fully developed turbulent jets impinging on the ground, as in VTOL aircraft [1], to the small-scale use of laminar jets to determine the shear strength of vascular tissue in the study of atherogenesis [2]. Impinging jets are also used in Chemical Vapor Deposition (CVD) processes [3, 4] and in the study of laminar flames [5–10]. Work has also been done on opposed-jet stagnation flow, a configuration widely used in combustion experiments [11–14]. Definitive experimental data for laminar impinging jets in the nozzle-to-plate separation distance L to nozzle-diameter d ratio (see Fig. 1) range of $0.5 \leq L/d \leq 1.5$ are not widely available. This range of L/d is useful in the study of strain-stabilized flames in combustion research. Available data in this range do not include detailed axial velocity profile measurements along the flow centerline, except for the study of Mendes-Lopes [7]. Such measurements are important in assessing one-dimensional flame models. This work focuses on the hydrodynamics of non-reacting impinging-jet flow, as a basis for related studies of strained flames [8–10].

Flow velocities in impinging jets have been measured by various means, such as Laser-Doppler Velocimetry (LDV) [12, 13] or Particle Image Velocimetry (PIV) [15]. In this study, Particle Streak Velocimetry (PSV) [9, 10, 16–18], a technique similar to particle tracking velocimetry [19], is used to obtain instantaneous flow-field measurements and, in particular, axial velocities along the flow centerline. A new PSV methodology has been implemented in this work that includes digital imaging, image processing, and new analysis techniques [9]. These improvements allow quantitative velocity data to be obtained throughout the flowfield with PSV, without excessive post-processing. This allows PSV to achieve accuracies that compete favorably with LDV or PIV, while providing advantages such as low particle mass loading, easy discrimination against agglomerated particles that may not track the flow, short run time experiments, and reliable velocity measurement from Lagrangian particle trajectories. The static (Bernoulli) pressure drop across the nozzle contraction is measured concurrently, providing measurement redundancy and a valuable independent parameter, as will be discussed below. The experimental data on impinging jets have been reported previously [8].

Impinging-jet flows have been described analytically, or simulated numerically, using different formulations and techniques. Schlichting [20] presents a one-dimensional axisymmetric model for an infinite-diameter jet impinging on a plate, which has been used in flame studies [5, 7]. This model was extended to allow both the velocity and velocity gradient to be specified at some distance from the stagnation plate [11, 21], providing a realistic and flexible boundary condition for finite nozzle-diameter impinging-jet flows. Two-dimensional, steady, axisymmetric calculations of viscous [2] and inviscid [1, 22–24] impinging-jet flow have also been performed. Except for the work of Strand [24], these calculations do not include nozzle-to-wall proximity effects.

In this work, the flow is modeled with varying levels of complexity: by means of an axisymmetric unsteady Navier-Stokes simulation, an axisymmetric potential-flow

formulation, and a one-dimensional streamfunction model. The first method is a spectral-element scheme [25, 26] that solves the incompressible axisymmetric Navier-Stokes equations. The unsteady spectral-element method is robust, and time- and space-accurate. The second method is a finite-difference potential-flow solution based on the classical ideal-jet approach [27, 28]. The potential- and viscous-flow calculations capture wall-proximity effects by including parts of the nozzle and plenum assembly in the computational domain. The one-dimensional model relies on a streamfunction formulation that is used in Chemical Vapor Deposition (CVD) studies [3, 4] and by the Combustion Community [5–7, 9, 11, 21].

The experimental results are used to evaluate the accuracy of the different simulation methodologies. Additionally, new scaling parameters and empirical properties of the centerline axial velocity field are discussed. The new scaling allows the identification of an analytical expression for the axial velocity profile of a laminar impinging jet for Reynolds numbers in the range $200 \leq Re \leq 1400$.

2 Experiments

In the experiments documented here, a room-temperature jet was generated in atmospheric pressure air from a contoured nozzle with an internal (nozzle-exit) diameter of $d = 9.9\,\mathrm{mm}$. The nozzle interior was designed by optimizing the inner radius profile, $r(x)$, through the contraction-section, expressed in terms of a 7^{th}-

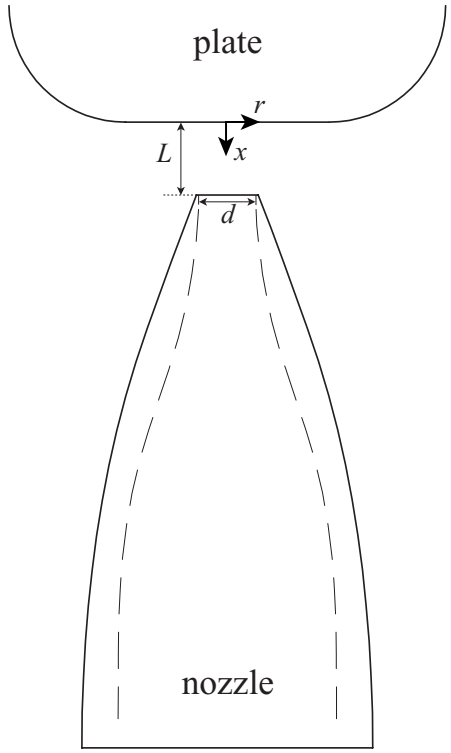

Figure 1: Experimental geometry.

degree polynomial, to minimize the exit boundary-layer displacement thickness and avoid the formation of Taylor-Görtler vortices in the concave section (*cf.* Fig. 1, and [29, 30]). The nozzle exterior was designed with attention to the upstream entrainment-induced flow, and to avoid flow separation and unsteadiness (Fig. 1). The air mass flux was controlled using a sonic metering valve. The flow was seeded with particles, using a seeder developed in-house, before entering the jet plenum, where screen and honeycomb sections were used for flow-uniformity and turbulence management. The nozzle-plenum system produced a uniform velocity profile in a free-jet configuration. The jet-exit velocity profile was measured with a flattened pitot probe ($d_{\mathrm{pitot}} \approx 0.4\,\mathrm{mm}$ in the radial direction) and an electronic-capacitance manometer (BOC Edwards W57401100) with a temperature-stabilized 1 torr differential-pressure transducer (BOC Edwards W57011419). Figure 2 compares the nozzle-exit velocity profile with the profile obtained from the two-dimensional viscous simulation, at a Reynolds number $Re_{\mathrm{j}} \equiv \rho\, d\, U_{\mathrm{j}}/\mu \cong 1400$, where U_{j} is the centerline velocity at the jet exit, ρ is the density, and μ is the viscosity. The profile is uniform, with less than 1% variation outside the wall boundary layers ($r/R \leq 0.6$, $R = d/2$). The slight disagreement between simulation and experiment in the wall boundary layer region is attributable to the finite pitot-probe extent in the radial direction d_{pitot}, for which no corrections were applied.

The jet was aligned normal to a solid wall (stagnation-plate assembly), at separation-distance to nozzle-diameter ratios of $L/d = 0.7$, 1.0, and 1.4. Significant changes in flow characteristics are observed over this L/d range. The stagnation plate was a cir-

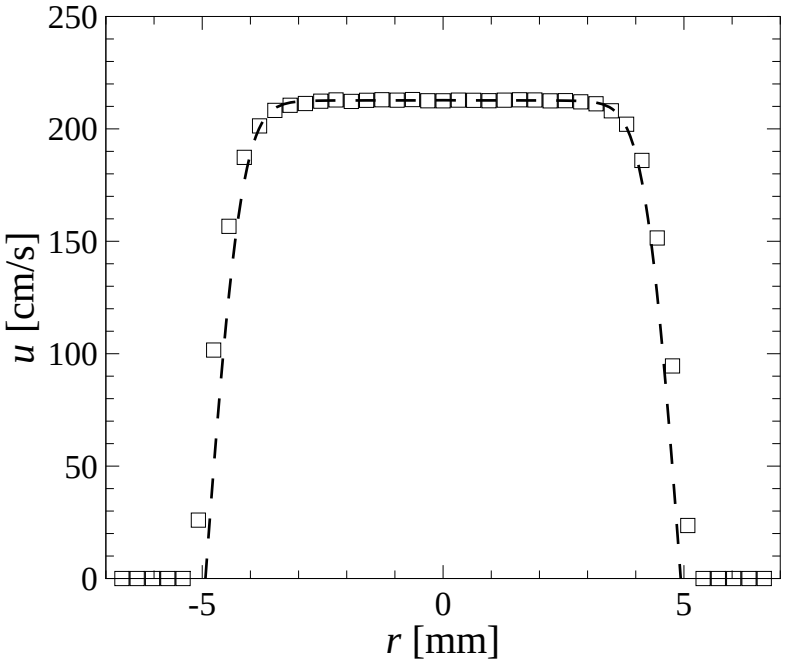

Figure 2: Nozzle-exit velocity profile ($d = 9.9\,\mathrm{mm}$, $Re_{\mathrm{j}} = 1400$). (□) experimental data. (dash line) viscous-simulation results. Pitot-probe internal opening was $d_{\mathrm{pitot}} \approx 0.4\,\mathrm{mm}$.

cular, copper block, 7.62 cm (3 in) in diameter and 5.08 cm (2 in) thick, with a 2.03 cm (0.8 in) bottom-edge radius. A bottom-edge radius was introduced to mitigate upstream effects of flow-separation and edge-flow unsteadiness in the stagnation-flow region (*cf.* Fig. 1).

PSV is well suited as a velocity-field diagnostic for this flow. In this axisymmetric, steady flow, the axial velocity component can be reliably measured on the centerline. Particle paths do not cross or overlap, and out-of-plane particle displacements are small and easily discernible when they occur (in-/out-of-focus streaks). The high sensitivity of the scattering cross section to particle size, in the size range employed, allows easy identification of agglomerates that may not track the high spatial-gradient regions in the flow. Streaks used for PSV processing were from in-plane, non-agglomerated particles. A single image frame can capture the entire velocity field, allowing PSV to be implemented in short-run-time experiments. A sample image of a cold-jet flow with particle streaks is reproduced in Fig. 3, for a nozzle-plate separation to nozzle-diameter ratio of $L/d = 1.0$. In this flow, the jet-nozzle centerline velocity is $U_\mathrm{j} = 106\,\mathrm{cm/s}$, yielding a Reynolds number, $Re_\mathrm{j} \cong 700$. The top and bottom portions of the laser sheet are masked to minimize scattering from the solid plate and nozzle surfaces.

In a variable-velocity field, particles will follow the flow if the dimensionless product of the local strain rate $\sigma = \mathrm{d}u/\mathrm{d}x$, and the Stokes time τ_S is small, *i.e.*, if,

$$\sigma\,\tau_\mathrm{S} \;\equiv\; \sigma\,\frac{\rho_\mathrm{p}\,d_\mathrm{p}^2}{18\,\mu} \;\ll\; 1\;. \tag{1}$$

Measurements relied on alumina particles (Al_2O_3; median size, $d_\mathrm{p} \cong 0.8\,\mu\mathrm{m}$, $\rho_\mathrm{p} \cong 3830\,\mathrm{kg/m^3}$; Baikowski Malakoff, RC-SPT DBM). At the maximum strain rates encountered in these experiments, $\sigma\,\tau_\mathrm{S} \cong 3 \times 10^{-3}$.

A Coherent I-90 Ar-ion (CW) laser, operated at $2 - 3\,\mathrm{W}$, was the illumination source. Two cylindrical lenses generated a thin laser sheet ($\approx 500\,\mu\mathrm{m}$) in the field of view. An Oriel chopper system (Model 75155), with a 50% duty-cycle wheel, modulated the laser beam. The chopper was placed at a horizontal waist in the laser beam to minimize chopping (on-off/off-on transition) times. Chopping frequencies were in the range, $0.5\,\mathrm{kHz} \le \nu_\mathrm{c} \le 2.4\,\mathrm{kHz}$, with ν_c optimized depending on flow velocity, in each case.

Image data were recorded with the in-house-developed "Cassini" [31] and "KFS" [32] digital-imaging systems. They are based on low-noise, 1024^2-pixel CCDs, on a $12\,\mu\mathrm{m}$ pitch. The Cassini camera is based on a CCD developed for the NASA Cassini mission. The KFS CCD was designed by M. Wadsworth and S. A. Collins of JPL. The camera heads and data-acquisition systems were designed and built by D. Lang at Caltech. Output for both is digitized to 12 bits/pixel. Magnification ratios were in the range of 1:1 – 1:1.5, using a Nikon 105 mm, $f/2.8$ macro lens. Exposure times were varied for optimum particle-streak density in the images, with framing rates for these experiments in the range of $8 - 10\,\mathrm{fps}$.

Small-particle streaks approximate Lagrangian trajectories of the flow (*cf.* Fig. 3). Local velocities $u(x)$, are estimated from streak pairs as $u(x) \cong \Delta X(x)/\Delta t$, yielding

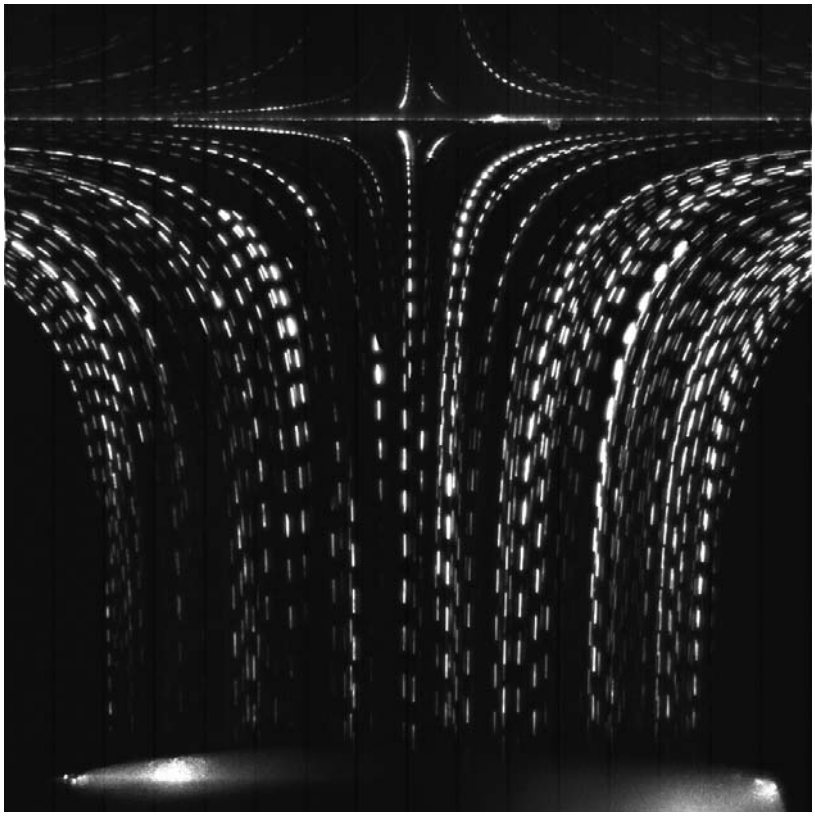

Figure 3: Impinging-jet flow. $Re_\mathrm{j} = 700$, $U_\mathrm{j} = 106\,\mathrm{cm/s}$, $L/d = 1.0$. Stagnation plate and nozzle exit are visible.

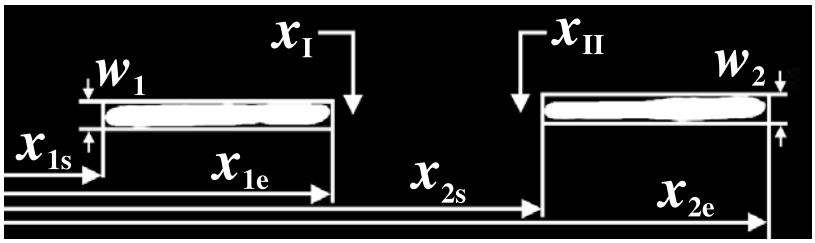

Figure 4: PSV measurement implementation.

$u_\mathrm{I} = L_\mathrm{I}/\tau_\mathrm{c}$ and $u_\mathrm{II} = L_\mathrm{II}/\tau_\mathrm{c}$, where $\tau_\mathrm{c} = 1/\nu_\mathrm{c}$ (reciprocal of chopper frequency) and $L_\mathrm{I} = x_\mathrm{2s} - x_\mathrm{1s}$ and $L_\mathrm{II} = x_\mathrm{2e} - x_\mathrm{1e}$ are the distances from the start/end of one streak to the start/end of the next, respectively (*cf.* Fig. 4). The velocity estimate, u_I, is located at $x_\mathrm{I} = (x_\mathrm{1s} + x_\mathrm{2s})/2 + (w_1 + w_2)/4$, where $x_{i\mathrm{s}}$ is the spatial location of the start of the i^th streak and w_i is the width of the i^th streak (*cf.* Fig. 4). Similarly, u_II is located at $x_\mathrm{II} = (x_\mathrm{1e} + x_\mathrm{2e})/2 - (w_1 + w_2)/4$, where $x_{i\mathrm{e}}$ is the location of the end of the i^th streak. Using the same intensity threshold on a streak pair removes systematic errors in applying the Lagrangian time interval τ_c. This methodology produces good agreement between velocity values derived from each streak pair. Streak lengths are estimated using bi-cubic fits on the 2-D streak-intensity image data, sampled to a 0.1-pixel resolution in both dimensions. An intensity threshold of approximately 0.4

of the maximum intensity of each streak is used to determine streak dimensions to this sampling resolution. The results are not sensitive to this choice and yield an overall PSV error of $< 0.01\,U_{\rm B}$.

The (Bernoulli) pressure difference between the jet plenum interior, at the straight section upstream of any contraction-section curvature, and the static pressure close to, but outside the jet-core flow region, was measured with an electronic-capacitance manometer (BOC Edwards W57401100) and a temperature-stabilized, 1 torr full-scale, differential-pressure transducer (BOC Edwards W57011419). Bernoulli and mass-flow data were acquired using the National Instruments LabView environment, synchronized to the digital-image acquisition to provide independent concurrent estimates of jet-exit velocity for every image. The Bernoulli velocity,

$$U_{\rm B} \;=\; \sqrt{\frac{2\,\Delta p/\rho}{1\;-\;(d/d_{\rm P})^4}}\;, \tag{2}$$

was then calculated, where Δp is the static pressure drop across the nozzle, ρ is the density of the jet fluid (air), d is the diameter of the nozzle exit, and $d_{\rm P}$ is the plenum diameter. At the flow velocities in this study, Bernoulli pressure differences were in the range of $0.1 - 3\,$Pa. At the lowest speeds investigated, an error of $< 0.01\,U_{\rm B}$ required an absolute measurement accuracy for the Bernoulli pressure drop of $\delta(\Delta p) \leq 2\times10^{-3}\,$Pa $= 2\times10^{-8}\,$bar. This accuracy is achievable with the differential-pressure tranducer employed if instrumental drifts and offsets are monitored. The Bernoulli pressure drop cannot be used to determine the jet-exit velocity for $L/d \leq 1$ because streamline curvature in the nozzle-exit plane produces a velocity deficit at the centerline [12]. However, the Bernoulli pressure drop is an important parameter for this flow, as discussed below. Mass flow rate was also measured concurrently (Omega FMA872-V-Air) providing an independent velocity estimate.

3 Numerical simulations

In this study, three different numerical simulations were performed at varying levels of complexity. The first is an axisymmetric viscous Navier-Stokes simulation, the second is a potential-flow calculation, and the third is a one-dimensional streamfunction formulation.

3.1 Axisymmetric Navier-Stokes formulation

The first numerical study relies on a spectral-element method [33] in an axisymmetric domain. The simulation code was developed by the authors and integrates the axisymmetric form of the Navier-Stokes equations, with appropriate boundary conditions as required to capture this flow, as discussed below. Only a limited number of studies have employed the spectral-element method to study this type of flow. Frouzakis et al. [14] utilized the spectral-element method to study the flowfield of opposed-jets and flames, rather than the impinging-jet flows studied here. In that

work, velocity boundary conditions were prescribed at the nozzle-exit locations. In this study, the inclusion of the nozzle interior/exterior allows nozzle-wall proximity effects, as well as entrainment, to be investigated.

The spectral-element method is a class of finite-element methods that can handle complex geometries. Additionally, this technique can achieve spectral accuracy by approximating the solution on Gauss-Lobatto-Legendre collocation points within each element. For elements adjacent to the axis, special Gauss-Radau-Legendre collocation points with a quadratic argument are utilized to achieve the appropriate parity for each field [34]. The code integrates a nondimensional form of the unsteady incompressible Navier-Stokes equations,

$$\nabla \cdot \mathbf{u} \;=\; 0 \;, \tag{3a}$$

$$\frac{\partial \mathbf{u}}{\partial t} \;=\; \mathbf{N}(\mathbf{u}) \;+\; \frac{1}{Re}\,\mathbf{L}(\mathbf{u}) \;-\; \nabla p \;, \tag{3b}$$

where the nonlinear term, $\mathbf{N}(\mathbf{u}) = -1/2\,[\mathbf{u}\cdot\nabla\mathbf{u} + \nabla\cdot(\mathbf{u}\mathbf{u})]$, is cast into the skew-symmetric form to reduce aliasing errors. The linear diffusion term is $\mathbf{L}(\mathbf{u}) = \nabla^2\mathbf{u}$.

Figure 5 shows the elements and boundary conditions used for $L/d = 1.424$. In the current simulations, 9^{th}- to 15^{th}-order polynomials are used in each element. These choices provide a balance between desired solution accuracy and reasonable computational time. These boundary conditions reasonably model the experimental

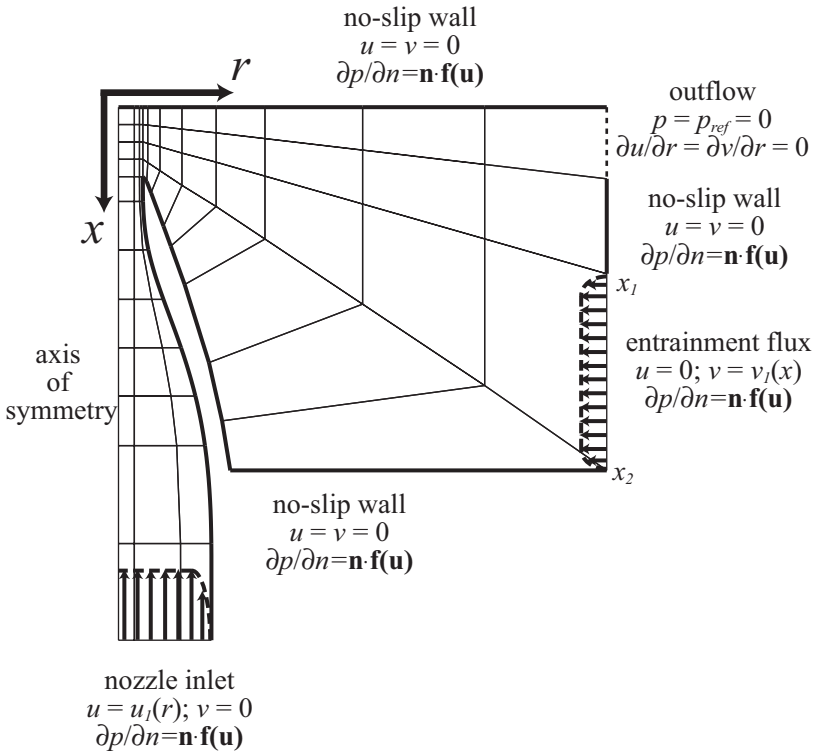

Figure 5: Axisymmetric Navier-Stokes simulation domain and boundary conditions. $\mathbf{f}(\mathbf{u}) = \nabla p = \mathbf{N}(\mathbf{u}) + \mathbf{L}(\mathbf{u})/Re$. $u_1(r)$ and $v_1(x)$ are the nozzle and entrainment inlet velocity profiles, respectively.

apparatus used in this study. The unsteady Navier-Stokes equations are integrated in time until the solution attains a steady-state condition, starting with the flow at rest in the domain interior.

A study of the effects of boundary conditions on the flowfield was undertaken to ascertain that the near-field solution was insensitive to the particular choices. A nearly flat velocity profile is introduced at the nozzle inlet (Fig. 5),

$$u_1(r)/U_\mathrm{P} = -\tanh[c_1(1 - r/r_\mathrm{P})] \,, \tag{4}$$

where $r_\mathrm{P} = d_\mathrm{P}/2$ is the radius of the plenum, U_P is the centerline velocity at the plenum, and c_1 was set to 50. This profile mimics the outflow from the turbulence-management section in the experiments. As expected, the jet profile at the nozzle exit is insensitive to the choice of inlet profile, owing to the high contraction ratio in the nozzle design (*cf.* Fig. 1).

To simulate the entrained flow, an entrainment flux Q_e, is introduced through the lower portion of the outer boundary. Over the range, $1/4 \le Q_e/Q \le 4$, where $Q = 2\pi \int_0^{r_\mathrm{P}} r\, u_1(r)\, \mathrm{d}r$ is the mass flux through the nozzle, the maximum difference in the velocity field was $0.008\, U_\mathrm{B}$ in the near-field region of interest ($0 \le r/d \le 1$, $0 \le x/d \le L/d$). For the entrainment flux (bottom right),

$$v_1(x)/U_\mathrm{P} = -\, c_2\, \tanh[c_3(x - x_1)(x_2 - x)/(x_2 - x_1)^2] \tag{5}$$

is specified (Fig. 5), with $c_2 = 0.0785$ and $c_3 = 50$. These choices yield $Q_\mathrm{e}/Q \approx 1.8$. A uniform-pressure condition is specified near the wall at the boundary of the domain exhaust, marked "outflow" in Fig. 5.

3.2 Potential-flow formulation

For axisymmetric flow, the continuity equation can be satisfied by expressing the velocity field in terms of a streamfunction, $\psi(x, r)$, *i.e.*,

$$u \;=\; \frac{1}{r}\,\frac{\partial \psi}{\partial r} \,, \qquad v \;=\; -\,\frac{1}{r}\,\frac{\partial \psi}{\partial x} \,. \tag{6}$$

In the absence of swirl, the azimuthal vorticity, ω, is related to the stream function by (*e.g.*, Batchelor [35]),

$$-\,r\,\omega \;=\; \frac{\partial^2 \psi}{\partial x^2} \,+\, \frac{\partial^2 \psi}{\partial r^2} \,-\, \frac{1}{r}\,\frac{\partial \psi}{\partial r} \;=\; r^2\,\frac{\mathrm{d}H}{\mathrm{d}\psi} \,, \tag{7}$$

where $H(\psi)$ is the Bernoulli constant,

$$H(\psi) \;\equiv\; \frac{1}{2}\,\left(u^2 \,+\, v^2\right) \,+\, \frac{p}{\rho} \,. \tag{8}$$

One approach to the inviscid impinging-jet problem is to specify an inlet axial velocity profile at some distance from the wall, determine $H(\psi)$ at that location, and then solve Eq. (7) in a domain bounded by the axis of the jet, the wall, and specified inlet

and outlet boundaries [1]. This approach is satisfactory provided the inlet conditions are not affected by the jet impingment.

In this study, we follow the conventional ideal-jet approach [27, 28], where the interior flow is irrotational, the shear-layers are infinitesimally thick, and the exterior flow is stagnant. Setting the right-hand side of Eq. (7) to zero, the equation for the streamfunction in the jet interior is then,

$$\frac{\partial^2\psi}{\partial x^2} + \frac{\partial^2\psi}{\partial r^2} - \frac{1}{r}\frac{\partial\psi}{\partial r} = 0 \; . \tag{9}$$

The surface of the jet is a streamline, hence $\psi(x_0, r_0) = \psi_0$, where ψ_0 is a constant and (x_0, r_0) are coordinates of any point on the surface of the jet. The location of the jet surface, (x_0, r_0), is not known a priori and must be determined as part of the solution, to satisfy the constant-pressure boundary condition,

$$u^2 + v^2 = \frac{1}{r^2}\left[\left(\frac{\partial\psi}{\partial x}\right)^2 + \left(\frac{\partial\psi}{\partial r}\right)^2\right] = U_{\rm B}^2 \; , \tag{10}$$

where $U_{\rm B}$ is the Bernoulli velocity. Schach [23] solved this problem using an integral equation approach, assuming the nozzle outflow was not affected by proximity to the wall. Strand [24] used a truncated series solution (up to four terms) to solve for two cases: $L/d \geq 1$ (ignoring wall-proximity effects) and $L/d \ll 1$. This approach, however, omits the transitional regime, $0.7 \leq L/d \leq 1.5$, of interest in this study.

The physical domain and boundary conditions are summarized in Fig. 6. Equation (9) was discretized using second-order centered finite differences on a fixed rectangular computational domain. This domain was mapped to the physical domain by the solution of two elliptic partial differential equations for the physical coordinates x and r. These equations were coupled to Eq. (9) through the boundary condition

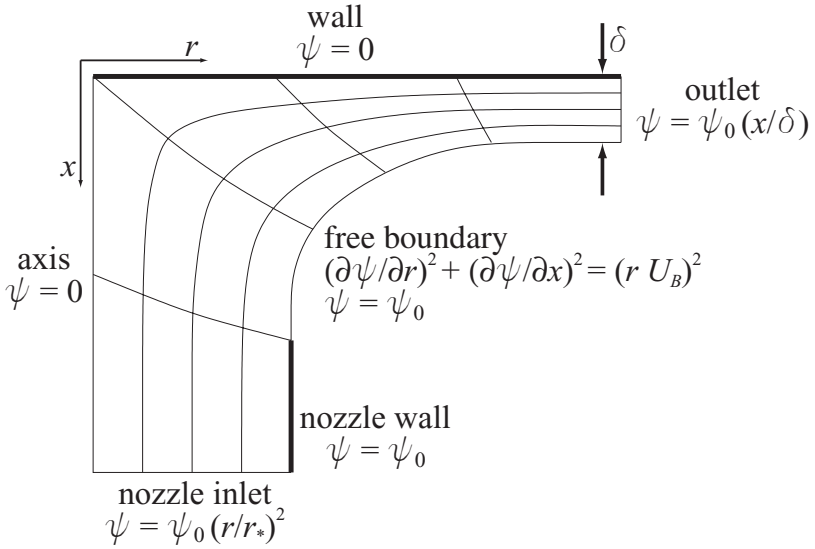

Figure 6: Potential-flow simulation domain and boundary conditions.

of Eq. (10). The simultaneous solution of these equations determines the shape of the free constant-pressure boundary. To capture wall-proximity effects, a constant-diameter nozzle is included in the computational domain. Instead of prescribing the nozzle radius, a finite velocity constraint is applied at the trailing edge of the nozzle. Indirectly, this allows the determination of the discharge coefficient C_V, originally defined by Strand [24], and given by,

$$C_V \;\equiv\; \frac{Q}{\pi\, r_*^2\, U_{\rm B}} \;. \tag{11}$$

where Q is the volume flow rate and r_* is the radius of the nozzle. Uniform axial and radial velocity profiles were prescribed at the inlet and outlet of the domain, respectively. The inlet and outlet were positioned about 4 and 8 nozzle radii from the wall stagnation point, respectively.

Second-order accuracy was verified by solving for infinite stagnation-point flow, on grids generated from the solution of the impinging-jet problem, at resolutions ranging from 20×80 to 80×320. The analogous plane-flow impinging-jet problem was also solved and compared to the analytic solution outlined by Birkhoff and Zarantonello [27]. The error in the discharge coefficient was less than 1% with excellent agreement between the numerical and analytic free boundaries. For the axisymmetric impinging-jet problem, convergence studies were conducted at resolutions ranging from 20×80 to 80×320. Differences in the centerline axial velocity were less than $0.01\,U_{\rm B}$. Sensitivity to the radial extent of the domain was studied by reducing the outlet radius to 4 nozzle radii. The difference in the centerline axial velocity was, again, less than $0.01\,U_{\rm B}$. The gradient of the centerline axial velocity decayed to almost zero at the nozzle inlet, indicating that the inlet was placed sufficiently far from the wall.

3.3 Streamfunction formulation

The one-dimensional solution for constant-density stagnation flows models the flow in terms of a local streamfunction $\psi(x,r) = r^2\,U(x)/2$, which leads to $u(x) = U(x)$ and $v(x,r) = -rU'(x)/2$ [*cf.* Eq. (6)]. The axisymmetric Navier-Stokes equations can then be expressed in terms of the axial velocity, $U(x)$, *i.e.*,

$$\nu\, U''' \;-\; U\, U'' \;+\; \frac{1}{2}\, U'^2 \;=\; -\,\frac{2\Lambda}{\rho}\;, \tag{12}$$

where Λ is termed the radial pressure eigenvalue of the problem,

$$\Lambda \;=\; \frac{1}{r}\,\frac{\partial p}{\partial r}\;, \tag{13}$$

and, in this formulation, must be a constant. The third-order ordinary differential equation requires three boundary conditions at $x = 0$. It is common to specify boundary conditions at $x = 0$ and $x = \ell$ with $0 < \ell \leq L$ some interior point, by adjusting the curvature boundary condition at $x = 0$ to achieve the desired boundary

condition at $x = \ell$. A fourth boundary condition can be satisfied by adjusting Λ,

$$\begin{array}{rcl} U(0) & = & 0 \\ U'(0) & = & 0 \\ U(\ell) & = & -U_\ell \\ U'(\ell) & = & -U'_\ell \, . \end{array} \tag{14}$$

Since $u(\ell, r) < 0$ (flow is towards the stagnation plate), the negative signs are chosen for convenience to make the constants U_ℓ and U'_ℓ positive. Plug-flow boundary conditions, *i.e.*, $U'(\ell) = 0$, at the nozzle exit plane, $\ell = L$, are commonly specified with this formulation. The inviscid outer solution to Eq. (12) is a parabola. In the inviscid limit, the flow is irrotational if $\Lambda = -\rho\,(U'_\ell)^2/4$, for which the solution reduces to pure stagnation flow where the coefficient of the curvature term is identically zero, *i.e.*, linear outer flow, $U'_\ell = U_\ell/\ell$. For more general boundary conditions, the resulting flow has vorticity, whereas the core of the experimental jet is irrotational. The introduction of vorticity to the flow is necessary to accomodate outer flows with curvature. The equations are solved using the *Cantera* software package [4].

4 Results and Discussion

Experimental velocity data reported here were recorded at three nominal Reynolds numbers,

$$Re \;\equiv\; \frac{\rho\, d\, U_{\rm B}}{\mu} \;\cong\; 400\,,\; 700\,,\; \text{and } 1400\;, \tag{15}$$

with actual values within ± 35, in each case, and at three nozzle-to-stagnation plate separation distance to nozzle-exit-diameter ratios, $L/d \cong 0.7$, 1.0, and 1.4. Figure 7 compares measured axial velocities, scaled by the Bernoulli velocity, for the three L/d ratios at the three Reynolds numbers. The velocity profiles collapse to a single curve, independent of L/d, if the axial velocity is scaled by the Bernoulli velocity. A centerline axial velocity deficit at the jet-exit develops as the separation distance is decreased due to the influence of the stagnation point on the nozzle flow [12]. Notably, the velocity and its gradient adjust to maintain self-similarity, with the Bernoulli velocity scaling the flow.

Figure 8 shows the axisymmetric viscous simulation results at $Re = 700$ and variable L/d. The velocity profiles follow a single curve when velocities are scaled by the Bernoulli velocity, consistent with the experimental results. Figure 9 compares the experimental data with the axisymmetric viscous calculations at $L/d = 1.4$ and $Re = 400$, 700, and 1400. The differences between experimental and numerical results for these three cases are less than $0.015\,U_{\rm B}$ root-mean-squared (rms), indicating that the experimental flowfield is adequately modeled. Figure 10 compares particle-streak-image data and streamlines from the axisymmetric viscous simulations. Good qualitative agreement can be seen, even in the entrainment region where the velocities are low ($< 0.02\,U_{\rm B}$).

Figure 11 compares the experimental data at the highest Reynolds number to the potential flow results. Here the axial distance is normalized by the effective diame-

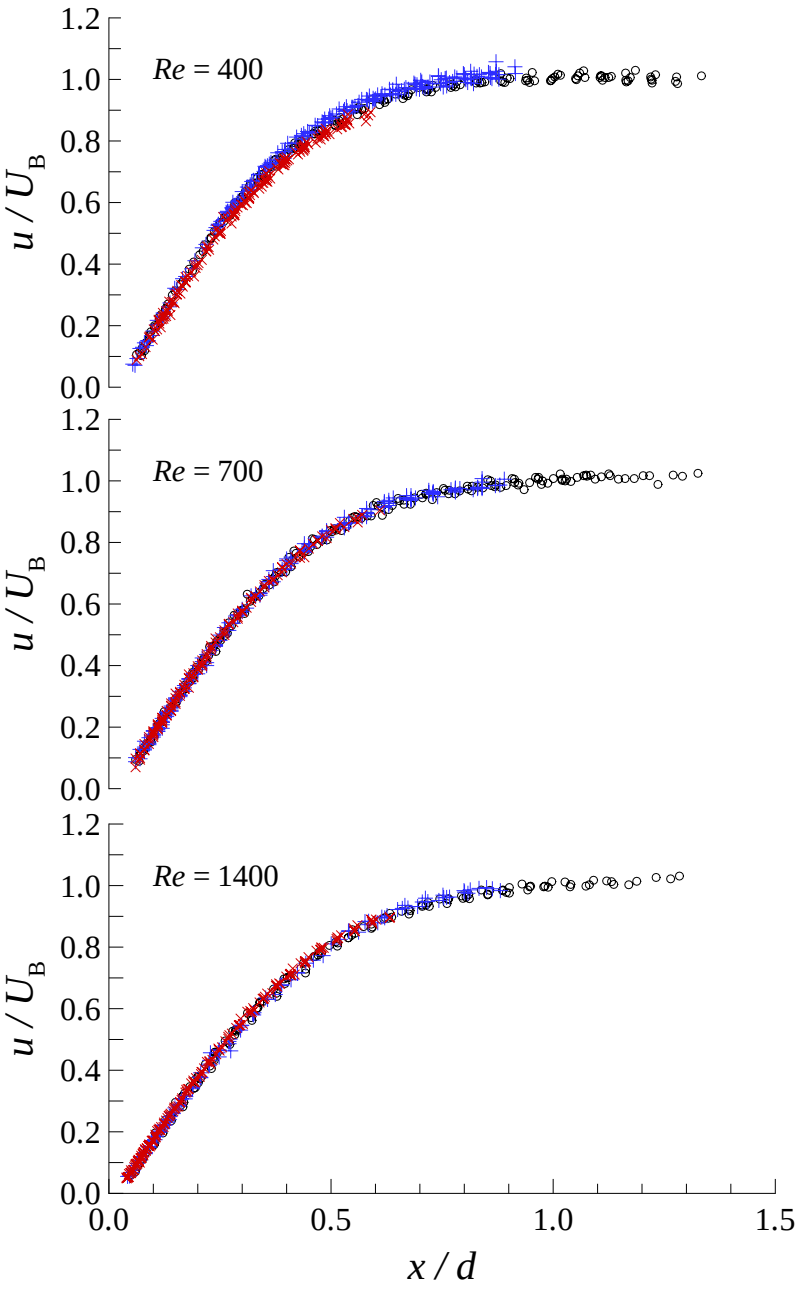

Figure 7: Comparison of velocity versus axial distance from plate at three nominal Reynolds numbers. Velocities are scaled by the Bernoulli velocity and axial distances by the nozzle diameter. Experimental results for separation distances of $L/d = 1.4$ ($\circ$), $L/d = 1.0$ ($+$), and $L/d = 0.7$ ($\times$).

ter d_*, where d_* is the nozzle diameter corrected for the nozzle-wall boundary-layer displacement thickness. One of the main effects of the Reynolds number in this flow is the change in the effective jet diameter through the boundary-layer displacement thickness. This effect should be removed before comparing the experiments to the inviscid potential flow results, which are valid in the limit of infinite Reynolds number.

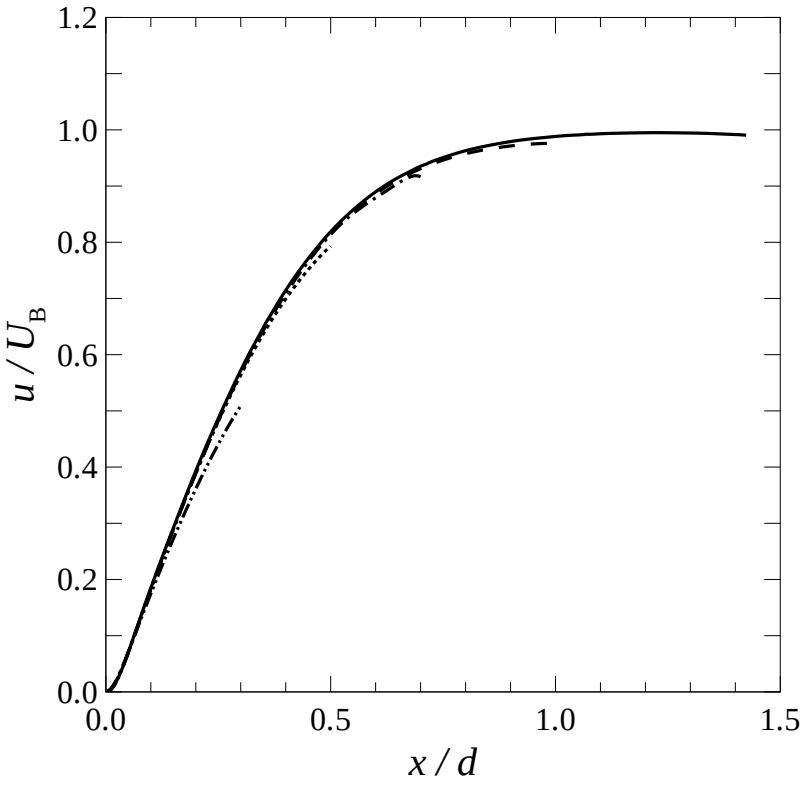

Figure 8: Scaled velocity versus axial distance from plate. Viscous calculations at $Re = 700$ and $L/d = 1.4$ (solid), 1.0 (dash), 0.7 (dash-dot), 0.5 (dotted), and 0.3 (dash-dot-dot).

The boundary layer thicknesses are estimated from axisymmetric viscous simulations of the nozzle flow. The small disagreement close to the wall is attributable to wall boundary layer displacement effects. This discrepancy leads to a difference in the maximum centerline axial velocity gradient. As with the experimental results, the axial velocity profiles collapse independent of L/d.

Experimental values of the discharge coefficient C_V [*cf.* Eq. (11)], were obtained from concurrent measurements of the Bernoulli pressure (yielding U_B) and the volumetric-flow rate Q. For large separation distances, the velocity outside the nozzle-wall boundary layers is essentially uniform and equal to U_B. The displacement-thickness-corrected radius $r_* = d_*/2$ can be estimated from $Q = \pi\, r_*^2\, U_\mathrm{B}$, where the values of U_B and Q are taken at large separation distances, $L/d \cong 1.5$. Figure 12 plots experimental and numerical values of C_V as a function of the normalized nozzle-wall separation distance L/d_*. These experiments are at constant mass flux and are reported in terms of the Reynolds number, based on the Bernoulli velocity measured at large separation distances, $Re_\infty = Re\,(L/d \gg 1)$. Estimates based on data from Strand [24], as well as his approximation of $C_V(L/d)$, for $L/d \ll 1$, are also included for comparison. The decrease of the discharge coefficient as the nozzle approaches the stagnation wall is attributable to the decrease in volume flow rate caused by the axial flow deceleration

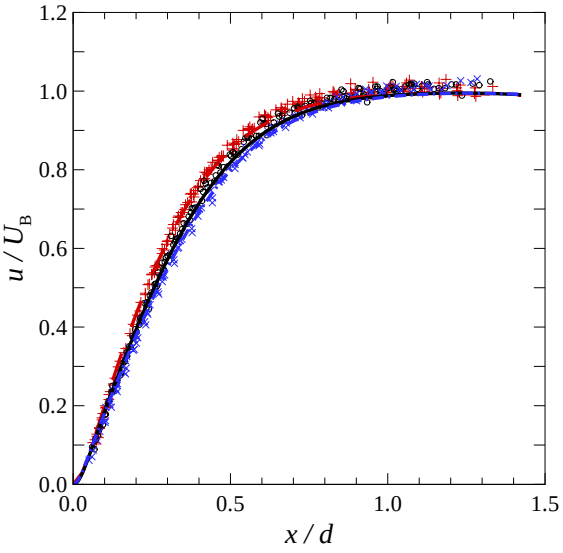

Figure 9: Scaled velocity versus axial distance from plate. Viscous calculations (lines) and experimental data (symbols) at $Re = 400$ (dash/+), 700 (solid/$\circ$), and 1400 (dash-dot/$\times$).

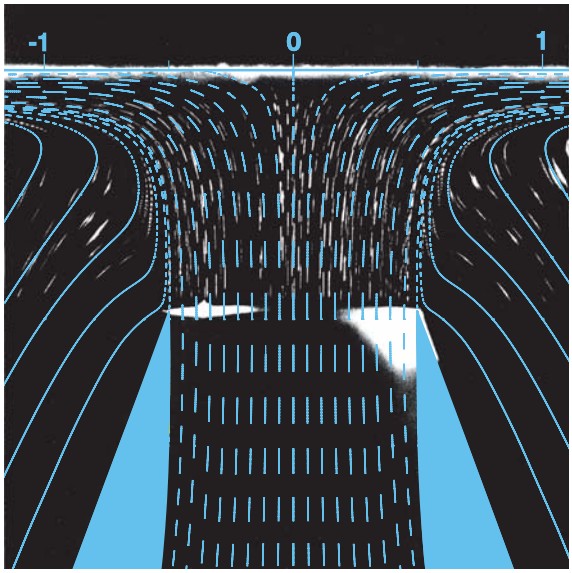

Figure 10: Particle streak image detailing entrained flow with superimposed axisymmetric viscous calculation (blue lines) at $Re = 700$ and $L/d = 1.0$.

(adverse pressure gradient) near the axis, at fixed Bernoulli pressure.

In the potential-flow solution, the constant-pressure streamline is tangential to the nozzle wall at the nozzle exit, for the speed on that streamline to remain finite. This means that the radial velocity must be zero at that point. The nozzle wall in the potential-flow solution corresponds to the displacement-thickness-corrected radius r_* in the viscous case. As this point is embedded within the nozzle-wall boundary-layer, the radial velocity need not be exactly zero, and the potential-flow constraint is relaxed. Viscous simulations show that the radial velocity, evaluated at r_*, is zero some distance upstream of the nozzle exit, say $x_{v=0}$. This suggests the (almost) irrotational inviscid core flow should have been well-approximated by potential flow, at some larger value of L/d_*, with the potential solution best compared to the viscous simulation at the same C_V. Matters are complicated because a portion of the streamline passing through $(x_{v=0}, r_*)$ is inside the physical pipe and the constant-pressure boundary condition used in the potential-flow calculation is no longer appropriate. For $Re_\infty = 700$ and $L/d_* = 0.57$, the radial velocity is zero at $x_{v=0}/d_* = 0.84$, which is not far from the potential-flow value of $L/d_* = 0.88$ that yields the same value of $C_V = 0.96$. For $Re_\infty = 700$ and $L/d_* = 0.34$, however, the radial velocity approaches zero at $x_{v=0}/d_* = 0.70$, whereas a potential-flow value of $L/d_* = 0.47$ is required to yield the same value of $C_V = 0.80$. In this discussion, the additional displacement effects of the boundary layers on the plate are not included.

Figure 13 compares the experimental axial velocity data, at $Re = 700$, to four different one-dimensional simulations, with plug-flow boundary conditions and different choices of the interior boundary location ℓ. Plug-flow boundary conditions

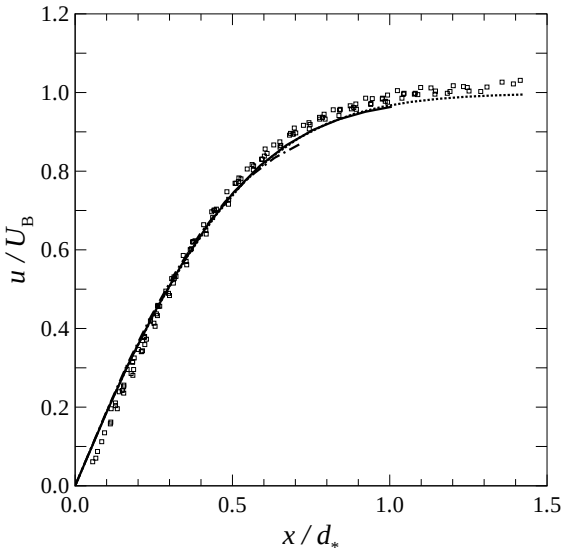

Figure 11: Velocity versus axial distance from plate normalized by the effective diameter d_*. Experimental data at $Re = 1400$ (□) and potential-flow simulations (lines) at $L/d_* = 1.4$ (dash), $L/d_* = 1.0$ (solid), and $L/d_* = 0.7$ (dash-dot).

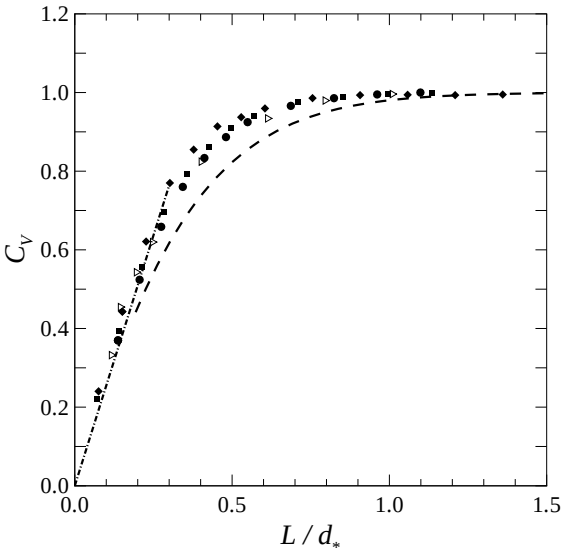

Figure 12: Discharge coefficient C_V *vs.* L/d_*. Experimental data at $Re_\infty = 400$ (◇), 1400 (□), and 2800 (○), potential-flow results (dash line), and data (▷) and theoretical curve (dash-dot line) by Strand [24].

capture the flow only for $\ell/d = 0.8$. This is due to the fact that the outer solution to the one-dimensional equations is a parabola and cannot capture the free-jet behavior (zero-gradient region of flow) that is exhibited for $x/d > 1.0$. Finite velocity gradients are evident for $x/d < 0.8$. The value of $\ell/d = 0.8$ is an intermediate case for which plug-flow boundary conditions capture the flow. The approximations invoked in arriving at the one-dimensional streamfunction model are valid in the limit of an infinite-diameter jet impinging on a surface. However, from Fig. 13 it appears that the model should be able to capture the flow in the region $0 \leq x/d < 0.8$ if appropriate boundary conditions are specified. The velocity and velocity-gradient boundary conditions at a given axial location, $U(\ell)$ and $U'(\ell)$, can be specified from an error-function fit to the experimental data [*cf.* Eq. (16)]. The one-dimensional solution calculated using this method at $Re = 700$, over the range $0.3 \leq \ell/d \leq 0.7$, has a maximum error of less than $0.03\,U_\mathrm{B}$, when compared to axisymmetric viscous simulations. Figure 14 shows the one-dimensional simulation results compared to experimental data at $Re = 700$, with boundary conditions taken from the experimental data at $\ell/d = 0.6$.

To further assess the one-dimensional models applicability to finite-nozzle diameter experiments, the axial velocity profiles from the axisymmetric-viscous simulations at several radii are presented in Fig. 15. The axial velocity profiles collapse for 20% of the radial domain, with only slight deviations observed at up to 60% of the nozzle-radius. At larger radial locations, the near-wall flow appears to be well characterized by the one-dimensional model. Radial velocity profiles are given in Fig. 16 as a func-

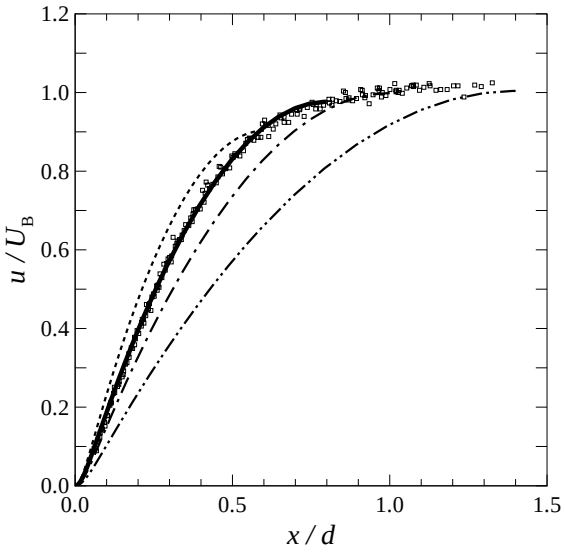

Figure 13: Comparison of streamfunction simulations with plug-flow boundary conditions (lines) to experimental results (□) at $Re = 700$, varying ℓ: $\ell/d = 0.6$ (dash), $\ell/d = 0.8$ (solid), $\ell/d = 1.0$ (dash-dot), $\ell/d = 1.4$ (dash-dot-dot).

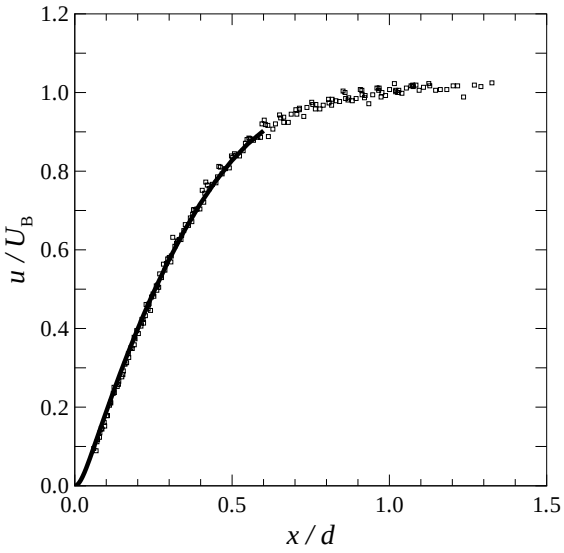

Figure 14: Comparison of streamfunction simulation (line) to experimental data (□) at $Re = 700$. Boundary conditions calculated from error-function fit to the data at $\ell/d = 0.6$.

tion of the axial distance from the wall. The one-dimensional model assumes a linear variation in the radial velocity with distance from the axis. The profiles are linear for more than 60% of the radial domain.

In their study of turbulent jets, Kostiuk et al. [13] showed that opposed- or impinging-jet velocity data are well characterized by an error function and used the parameters obtained from the error-function fit to collapse their experimental data. Their error function contained three adjustable parameters, the velocity at infinity U_∞, a strain-rate parameter α, and a wall-offset length δ/d,

$$\frac{u(x)}{U_\infty} \;=\; \mathrm{erf}\left[\,\alpha\,\left(\frac{x}{d} \,-\, \frac{\delta}{d}\right)\,\right] \;. \tag{16}$$

The collapse of the experimental and numerical data discussed above suggests that the appropriate velocity scale for laminar impinging jets is the Bernoulli velocity, *i.e.*, $U_\infty = U_\mathrm{B}$. From one-dimensional viscous stagnation-flow theory (*cf.* [10]), the scaled-offset length δ/d, which is proportional to the scaled-wall-boundary-layer thickness, can be related to the strain-rate parameter α, such that,

$$\frac{\delta}{d}(Re,\alpha) \;=\; 0.755\,\sqrt{\frac{1}{Re\,\alpha}} \;. \tag{17}$$

Thus, the only free parameter in this error-function fit to the data is the strain-rate parameter α, which should be a function of Reynolds number alone, *i.e.*, $\alpha = \alpha(Re)$.

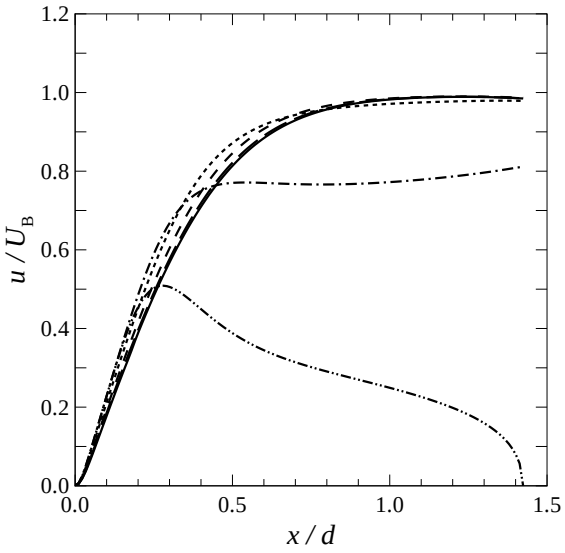

Figure 15: Axial velocity versus axial distance from plate at radial locations of $r/R = 0$ (solid), $r/R = 0.2$ (long-dash), $r/R = 0.4$ (dash), $r/R = 0.6$ (dot), $r/R = 0.8$ (dash-dot), and $r/R = 1.0$ (dash-dot-dot). $Re = 700$ and $L/d = 1.4$.

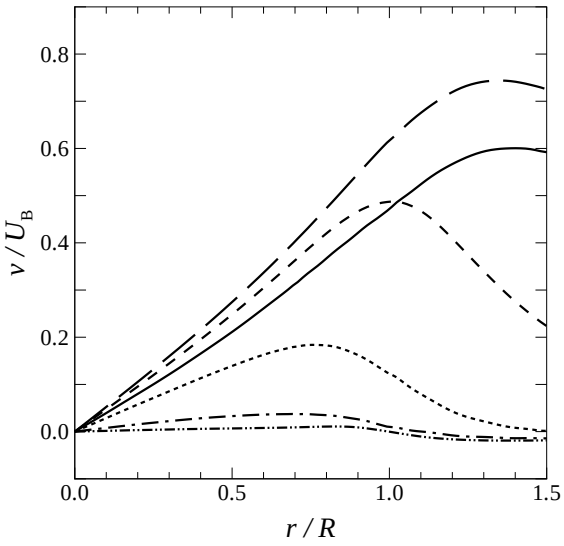

Figure 16: Radial velocity versus radial distance at axial locations of $x/d = 0.01$ (solid), $x/d = 0.1$ (long-dash), $x/d = 0.2$ (dash), $x/d = 0.4$ (dot), $x/d = 0.7$ (dash-dot), and $x/d = 1.0$ (dash-dot-dot). $Re = 700$ and $L/d = 1.4$.

Therefore, the axial velocity field for an axisymmetric impinging laminar jet is fully specified by the Bernoulli velocity U_B, since the Reynolds number is, in turn, derived from it.

The error-function fit to the data at $Re = 1400$ is plotted in Fig. 17. The error function was fit to each experimental and viscous simulation case by adjusting α such that the root-mean-squared (rms) error was minimized. For each Reynolds number, the strain-rate parameter α was averaged over the range $0.7 \leq L/d \leq 1.4$. This single $\alpha(Re)$ dependence was subsequently used in all error-function fits to determine the resulting rms error $\epsilon_{\rm rms}$. The fit parameters and $\epsilon_{\rm rms}$ are shown in Table 1.

As previously mentioned, the main Reynolds number effect for this flow is through the nozzle-wall boundary-layer thickness. To account for this effect, the displacement-thickness-corrected diameter d_* is an appropriate scaling parameter for axial distances. Figure 18 shows the scaled velocity profiles from axisymmetric viscous simulations at four Reynolds numbers. For low Reynolds numbers ($Re = 200$) viscous losses result in a jet-exit velocity that is less than the Bernoulli velocity. There is an additional weak Reynolds number effect exhibited for $Re = 200$ and 400 that is not fully captured by the current scaling and is manifested in the slope of the profiles. However, the velocity profiles collapse reasonably well using this scaling, and this allows the specification of an analytical expression for the velocity profile of the

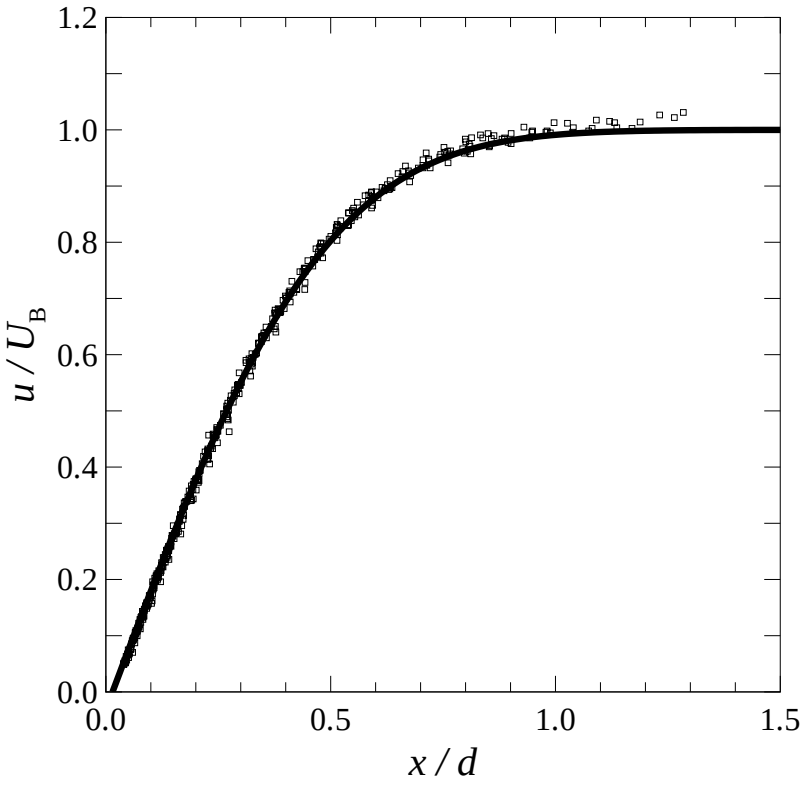

Figure 17: Comparison of error-function fit (line) to experimental data (□) at $Re = 1400$.

Table 1: Error-function fit parameters and rms error $\epsilon_{\rm rms}$ of fits to experimental and viscous-simulation data.

			Experiment	Simulation
Re	α	δ/d	$\epsilon_{\rm rms}/U_{\rm B}$	$\epsilon_{\rm rms}/U_{\rm B}$
400	2.21	0.027	0.017	0.014
700	2.00	0.020	0.010	0.009
1400	1.88	0.015	0.011	0.010

impinging jet in this Reynolds number range, *i.e.*,

$$\frac{u(x)}{U_{\rm B}} \;=\; {\rm erf}\left[\alpha_* \left(\frac{x}{d_*} - \frac{\delta}{d_*}\right)\right] \;, \tag{18}$$

where $\alpha_* = 1.7$, and $\delta/d_* = 0.016$ were found from fitting this error function to the axisymmetric-viscous-simulation data. The rms error of the error-function fit is less than 0.5% for $Re = 700$ and 1400 and less than 2% for $Re = 200$ and 400. In the limit of infinite Reynolds number, the wall boundary-layer thickness will tend to zero, and the potential flow formulation will accurately model the flow. In this limit, the velocity field is given by $u/U_{\rm B} = {\rm erf}\left[\alpha_{\rm p}\,(x/d_*)\right]$, with $\alpha_{\rm p} = 1.59$ found by fitting this

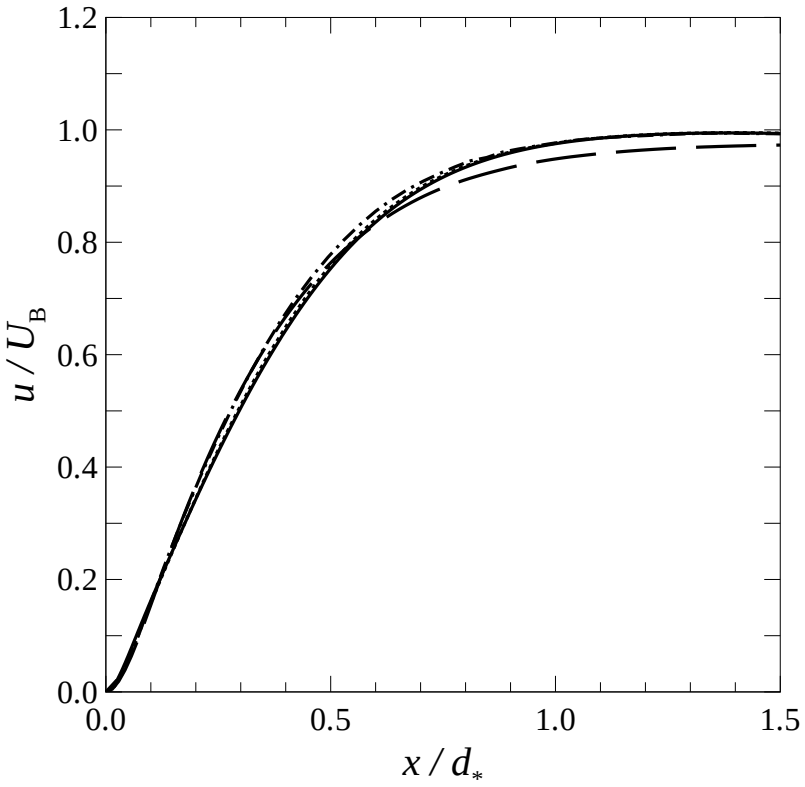

Figure 18: Axisymmetric-viscous simulation velocity profiles versus axial distance from plate normalized by the effective diameter d_* at $L/d = 1.4$ and $Re = 200$ (long dash), 400 (dash-dot), 700 (dot), and 1400 (solid).

error function to the potential flow simulations. These expressions yield the velocity profile for an impinging jet with a measurement of the Bernoulli pressure across the nozzle contraction, the gas density and viscosity, the diameter ratio of the nozzle inlet and outlet, and the boundary layer thickness at the nozzle exit.

Using Eq. (16), the strain rate at any point on the axis can be computed using the error-function fit,

$$\sigma(x) \;=\; \frac{\mathrm{d}u(x)}{\mathrm{d}x} \;=\; \frac{2U_\mathrm{B}\alpha}{\sqrt{\pi}d}\,\exp\left[-\alpha^2\left(\frac{x}{d}-\frac{\delta}{d}\right)^2\right] \;. \tag{19}$$

This yields a maximum strain rate of $\sigma_\mathrm{max} = 2U_\mathrm{B}\alpha/\sqrt{\pi}d$, at $x = \delta$. This is an important quantity in the ignition of stagnation-flow-stabilized premixed flames and in assessing the ability of particulate markers to track the flow [*cf.* Eq. (1)].

5 Conclusions

Scaling the centerline axial velocity for an impinging jet by the Bernoulli velocity, calculated from the static pressure drop across the nozzle contraction, collapses centerline axial-velocity data on a single curve that is independent of the nozzle-plate

separation distance for separation-to-diameter ratios of $L/d \geq 0.5$. The axisymmetric viscous and potential-flow simulations reported here allow nozzle-wall proximity effects to be investigated by including the nozzle in the solution domain. Using this simulation domain, axisymmetric viscous simulations yield good agreement with experiment and confirm the velocity profile scaling. The potential-flow simulations reproduce the collapse of the data, however, at these Reynolds numbers, viscous effects result in disagreement with experiment. One-dimensional streamfunction simulations provide an adequate approximation of the flow in the stagnation region if the boundary conditions are correctly specified.

The scaled axial velocity profiles are well-characterized by an error function with one Reynolds-number dependent parameter α. The error function provides a good fit to both experimental and viscous-simulation data, with root-mean-squared errors of $\epsilon_{\text{rms}} \lesssim 0.02\,U_{\text{B}}$. In this Reynolds number range, viscous effects are captured by scaling the axial distance by the effective (displacement-thickness-corrected) diameter d_*. This scaling relies on thin nozzle boundary layers (d_*/d close to unity) and negligible viscous losses through the nozzle. These scalings allow the specification of an analytical expression for the velocity profile of an impinging laminar jet over the Reynolds number range of $200 \leq Re \leq 1400$.

6 Acknowledgments

We would like to thank D. Lang for his contributions to the digital-imaging in this work, as well as G. Katzenstein for his assistance with experimental design and assembly. R. D. Henderson and H. Blackburn provided considerable assistance, as well as the codes that our axisymmetric viscous simulation code is based on. The work was funded by AFOSR Grant F49620–01–1–0006 and the DOE Caltech ASC Contract W–7405–ENG–48, whose support is gratefully acknowledged.

References

[1] A. Rubel. Inviscid axisymmetric jet impingement with recirculating stagnation regions. *AIAA J.*, 21:351–357, 1983.

[2] M. D. Deshpande and R. N. Vaishnav. Submerged laminar jet impingement on a plane. *J. Fluid Mech.*, 114:213–236, 1982.

[3] C. Houtman, D.B. Graves, and K.F. Jensen. CVD in stagnation point flow - an evaluation of the classical 1D-treatment. *J. Electrochem. Soc.*, 133(5):961–970, 1986.

[4] D. G. Goodwin. An open-source, extensible software suite for CVD process simulation. In *Proc. of CVD XVI and EuroCVD Fourteen,* Electrochem. Soc., pages 155–162, 2003.

[5] H. W. Smith, R. A. Schmitz, and R. G. Ladd. Combustion of a premixed system in stagnation flow–i. theoretical. *Comb. Sci. Technol.*, 4:131–142, 1971.

[6] M. Fang, R. A. Schmitz, and R. G. Ladd. Combustion of a premixed system in stagnation flow–ii. experiments with carbon monoxide oxidation. *Comb. Sci. Technol.*, 4:143–148, 1971.

[7] J. M. C. Mendes-Lopes. *Influence of strain fields on flame propagation*. PhD thesis, Cambridge University, 1983.

[8] J. M. Bergthorson, D. G. Goodwin, and P. E. Dimotakis. Experiments and modeling of impinging jets and premixed stagnation flames. In M. Behnia, W. Lin, and G. D. McBain, editors, *Proceedings of the Fifteenth Australasian Fluid Mechanics Conference*, number AFMC00087, 2004. `www.aeromech.usyd.edu.au/15afmc`.

[9] J. M. Bergthorson, D. G. Goodwin, and P. E. Dimotakis. Particle streak velocimetry and CH laser-induced fluorescence diagnostics in strained, premixed, methane-air flames. *Proc. Comb. Inst.*, 30:1637–1644, 2005.

[10] J. M. Bergthorson. *Experiments and modeling of impinging jets and premixed hydrocarbon stagnation flames*. PhD thesis, California Institute of Technology, 2005.

[11] R. J. Kee, J. A. Miller, G. H. Evans, and G. Dixon-Lewis. A computational model of the structure and extinction of strained, opposed flow, premixed methane-air flames. *Proc. Comb. Inst.*, 22:1479–1494, 1988.

[12] J. C. Rolon, D. Veyante, J. P. Martin, and F. Durst. Counter jet stagnation flows. *Exp. Fluids*, 11:313–324, 1991.

[13] L. W. Kostiuk, K. N. C. Bray, and R. K. Cheng. Experimental study of premixed turbulent combustion in opposed streams: Part I - non-reacting flow field. *Comb. Flame*, 92:377–395, 1993.

[14] C. E. Frouzakis, J. Lee, A. G. Tomboulides, and K. Boulouchos. Two-dimensional direct numerical simulation of opposed-jet hydrogen-air diffusion flame. *Proc. Comb. Inst.*, 27:571–577, 1998.

[15] C. C. Landreth and R. J. Adrian. Impingement of a low reynolds number turbulent circular jet onto a flat plate at normal incidence. *Exp. Fluids*, 9:74–84, 1990.

[16] P. E. Dimotakis, F. D. Debussy, and M. M. Koochesfahani. Particle streak velocity field measurements in a two-dimensional mixing layer. *Phys. Fluids*, 24: 995–999, 1981.

[17] J. C. Agüí and J. J. Jiménez. On the performance of particle tracking. *J. Fluid Mech.*, 185:447–468, 1987.

[18] C. M. Vagelopoulos. *An experimental and numerical study on the stability and propagation of laminar premixed flames*. PhD thesis, University of Southern California, 1999.

[19] T. Echekki and M. G. Mungal. Flame speed measurements at the tip of a slot burner: Effects of flame curvature and hydrodynamic stretch. *Proc. Comb. Inst.*, 23:455–461, 1990.

[20] H. Schlichting. *Boundary layer theory*. McGraw-Hill Book Company, Inc., New York, 1960.

[21] R. J. Kee, M. E. Coltrin, and P. Glarborg. *Chemically Reacting Flow - Theory & Practice*. John Wiley & Sons, Inc., New Jersey, 2003.

[22] D. J. Phares, G. T. Smedley, and R. C. Flagan. The inviscid impingement of a jet with arbitrary velocity profile. *Phys. Fluids*, 12:2046–2055, 2000.

[23] W. Schach. Deflection of a circular fluid jet by a flat plate perpendicular to the flow direction. *Ingenieur-Archiv*, 6:51–59, 1935.

[24] T. Strand. On the theory of normal ground impingement of axisymmetric jets in inviscid incompressible flow. *AIAA Paper*, 64:424, 1964.

[25] R. D. Henderson and G. E. Karniadakis. Unstructured spectral element methods for simulation of turbulent flows. *Journal of Computational Physics*, 122:191–217, 1995.

[26] G. E. Karniadakis and S. J. Sherwin. *Spectral/hp element methods for CFD*. Oxford University Press, New York, 1999.

[27] G. Birkhoff and E. H. Zarantonello. *Jets, Wakes and Cavities*. Academic Press, New York, 1957.

[28] M. I. Gurevich. *Theory of jets in ideal flows*. Academic Press, New York, 1965.

[29] P. G. Drazin and W. H. Reid. *Hydrodynamic Stability*. Cambridge University Press, New York, 1981.

[30] D. R. Dowling. *Mixing in gas phase turbulent jets*. PhD thesis, California Institute of Technology, 1988.

[31] J. W. Shan and P. E. Dimotakis. Turbulent mixing in liquid-phase transverse jets. *GALCIT Fluid Mechanics Report No. 2001.006, 2001*, unpublished. URL `http://resolver.library.caltech.edu/CaltechGalcitFM:2001.006`.

[32] B. Kern, D. B. Lang, C. Martin, P. E. Dimotakis, and M. Wadsworth. A high-speed quadrature-phase rotation-shearing interferometer for imaging through turbulence. *AIAA Paper*, 2001:2797, 2001.

[33] Patera, A. T. A spectral element method for fluid dynamics: Laminar flow in a channel expansion. *Journal of Computational Physics*, 54:468–488, 1984.

[34] A. Leonard and A. Wray. A new numerical method for the simulation of three-dimensional flow in a pipe. In *Lecture Notes in Physics, No. 170: Eighth international conference on numerical methods in fluid dynamics*, pages 335–342. Springer-Verlag, New York, 1982.

[35] G. K. Batchelor. *An Introduction to Fluid Dynamics*. Cambridge University Press, New York, 1967.